LAWRENCE
LIVERMORE
NATIONAL
LABORATORY

LLNL-JRNL-847264

Localized Keyhole Pore Prediction during Laser Powder Bed Fusion via Multimodal Process Monitoring and X-ray Radiography

S. Gorgannejad, A. A. Martin, J. Wang, M. Strantza, G. M. Guss, S. Khairallah, J. B. Forien, V. Thampy, S. Liu, P. Quan, C. J. Tassone, N. P. Calta

April 6, 2023

Additive Manufacturing

Disclaimer

Localized Keyhole Pore Prediction during Laser Powder Bed Fusion via Multimodal Process Monitoring and X-ray Radiography

Sanam Gorgannejad[a],* Aiden A. Martin[a], Jenny W. Nicolino [a], Maria Strantza [a], Gabriel M. Guss [a], Saad Khairallah [a], Jean-Baptiste Forien [a], Vivek Thampy[b], Sen Liu [b], Peiyu Quan [b], Christopher J. Tassone [b], and Nicholas P. Calta[a]

[a] Lawrence Livermore National Laboratory, Livermore, California, 94550, USA
[b] Stanford Synchrotron Radiation Lightsource, SLAC National Accelerator Laboratory, Menlo Park, California, 94025, USA
*email: gorgannejad1@llnl.gov

Abstract

Systematic fault detection and control during laser powder bed fusion (L-PBF) has been a long-standing objective for system manufacturers and researchers in the additive manufacturing (AM) industry. This manuscript investigates a data fusion approach for detection of keyhole porosity formation during laser irradiation of Ti-6Al-4V substrates by concurrent recording of thermally induced optical emission measured using both off-axis and coaxial photodiode sensors, and acoustic emission. Subsurface defect formation was monitored via high-speed synchrotron X-ray imaging at 20,000 frames per second, enabling temporal registration of keyhole pore formation events to the monitoring signals at a resolution of 50 µs. We developed data fusion machine learning (ML) models for localized prediction of keyhole pore formation at various time scales ranging from 0.5 ms to 2 ms. The signal segments were featurized using two independent approaches: (1) power spectral density (PSD) and (2) highly comparative time series analysis (HCTSA) framework. The extracted features from different sensor modalities were fused together to construct a multimodal feature space and sequential feature selection was used to determine the most informative features for training the ML models. The predictive performance was evaluated for three classifying algorithms: Support Vector Machine (SVM), K-Nearest Neighbor (KNN), and Gaussian Naïve Bayes (GNB). As a result, pore formation events were predicted with up to 0.95 F1-score, 1.0 recall and 0.94 accuracy. The most heavily weighted features indicate that model performance is chiefly governed by the acoustic monitoring signal, with a secondary contribution from the optical emission sensors.

1. Introduction

The technological advancements in the field of metal laser powder bed fusion (L-PBF), over the past decade have created a strong urge in many manufacturing sectors for adoption of additive manufacturing (AM). However, production of industrial-scale components with high degree of geometrical flexibility while ensuring superior quality and reproducibility, is a persistent challenge [1, 2]. For the L-PBF technique, over fifty parameters are reported to impact the process [3]. The high level of complexity and interconnectivity between parameters, as well as the stochastic nature of L-PBF, presents a challenge for quality control of L-PBF-produced parts [4]. One promising route to help address this issue is the development of robust in situ process monitoring approaches to ensure part quality during fabrication.

Among all the commonly occurring discontinuities and defects (e.g., cracking, balling, delamination, and excess surface roughness), pores are the most prevalent and drastically compromise densification and mechanical properties of the printed components [5, 6]. They are categorized into three primary groups: (1) lack of fusion pores – insufficient heat input leading to voids between consecutive layers, (2) keyhole pores – excessive heat input resulting in deep and narrow depression that can create pores in multimodal regime [7], and (3) gas entrapped pores – failure of gas within the powder feedstock to escape before solidification [8, 9]. This paper focuses on keyhole pores and will not cover other types of process-induced voids.

Recently, in situ sensing approaches, such as acoustic emission spectroscopy [10, 11], whole-layer imaging [12, 13], high-speed infrared (IR) and near-IR imaging [14-16], high-speed X-ray imaging [17-19], thermionic emission [20], and pyrometry [21, 22], have been widely adopted to monitor the build process and perform real-time quality control and flaw detection [21, 22].

Successful application of acoustic emissions for process monitoring has been demonstrated for a range of different laser-based manufacturing techniques such as directed energy deposition (DED) [23-25], laser welding [26, 27], and L-PBF [28, 29]. When an acoustic source generates sound waves, they propagate as pressure variations in the surrounding medium that can be detected by microphones. This monitoring approach relies on acoustic signatures generated by keyhole instability and variations in plasma density within the vapor plume. Any change in laser energy density that introduces critical instability at the keyhole will influence vaporization and consequently result in plasma, air density, and surface wave fluctuations in the vicinity of the melt pool that in turn lead to signals collected by the monitoring microphone [10, 30], although the mechanistic details of precise linkages between fluctuation types and observed acoustic signatures is an area of active research. Shevchik et al. [31] used acoustic emission and convolutional neural networks (CNN) to classify samples into poor, medium, and high-quality classes that were defined based on their pore content. The algorithm classified samples with a maximum accuracy of 89%. Pandiyan et al. [32] applied two CNN architectures to train approximately 16,000 acoustic time series segments of 5 ms length which were collected during line track lasing of Inconel 718. The models were able to differentiate anomalous segments, including defects such as balling, lack of fusion, and keyhole pores from the reference conduction mode regimes with 96% accuracy. In another study by Tempelman et al. [33], keyhole pore formation was detected on single laser tracks with an accuracy of 97% over a window size of 7.5 ms acoustic time series. Various signal featurization approaches permitted the employment of a simple machine learning (ML) algorithm instead of complex and computationally expensive Neural Network (NN) models.

Optical sensing approaches have also been widely investigated in literature using many approaches including both coaxial and off-axis photodiodes, pyrometers, and IR cameras to collect surface temperature and geometry of the melt pool. Forien et al. [34], revealed the increased probability of pore creation with thermal monitoring signals and demonstrated the derivation of process signatures signifying conduction to keyhole transition. Mitchell et al. [35] showed that the in situ pyrometry data effectively identifies melt pool outlier/anomalous signatures and holds a direct linkage with both intentional cavities and unintentional porosities within the printed part. Zouhri et al. [36] classified parts printed at different density levels using a coaxial pyrometer data and

achieved accuracy of 90%. Similar studies have shown build density classification and prediction by employing photodiode sensor signals with various supervised, unsupervised, and semi-supervised ML techniques [37, 38].

Beyond single-sensor approaches, multimodal monitoring systems are more successful in capturing the complexity of deeply intertwined physical phenomena during defect creation [39, 40]. The use of two sources of image-based sensor data, high-speed video camera and temperature field imaging system, showed significant improvement in reducing the false positive rates in prediction of the part quality categories when compared to a single data source [41]. Templeman et al. reported a sensor fusion model comprising of pyrometry and acoustic signals which provided improved predictions of keyhole porosity when compared to a single sensor, although the effectiveness of individual sensor data in enhancing model prediction varied [42]. Post-build fusion of the layer wise build imagery, acoustic and multi-spectral emissions with scan vector trajectory data established a binary classifier with accuracy of 98.5% for detecting the flaws as indicated by X-ray CT scans [43]. A deep learning based model achieved an accuracy of 98% in predicting lack of fusion, conduction and keyhole mode at short time scale ranging from 0.5 ms to 4 ms using the monitoring signal collected from a four-sensor system that incorporates acoustic, back reflection, visible, and infrared sensors [18].

Instantaneous and local prediction of the keyhole porosity generation has been a prolonged challenge. One of the primary hurdles is that registration of the pore formation events to the time series sensing signals at short time- and length-scales is bounded by the stochastic nature of the keyhole pore formation. Martin et al. [44] have shown the existence of an offset between pore locations at the time of formation and after solidification, attributed to the rapid movement of the pores inside the melt pool tail. Clearly, post-build spatial and temporal registration using X-ray CT scans are inadequate in providing such high-fidelity information. As a result, the majority of the defect detection efforts via in situ sensing are primarily focused on full part or layer scales. Accordingly, in this work we employed high-speed in situ synchrotron X-ray imaging to determine pore formation times with tens of microsecond accuracy. In a similar research, Ren et al. [45] demonstrated the use of synchrotron X-ray and thermal imaging to reach prediction temporal resolution below 1 ms for detection of the keyhole pores.

Extracting an explicit correlation between the raw sensor signals and the physical phenomenon, such as pore formation, that takes place during the laser fusion process, is implausible due to the complexity and stochastic nature of these phenomena. Feature extraction or signal featurization therefore plays a pivotal role in priming the monitoring measurements for developing interpretable ML models that not only possess predictive capability but also allow for gaining insight into the governing pore formation mechanisms. Featurization transforms the raw data into numerical features to unveil hidden patterns and signal characteristics [46]. Different featurization schemes extract unique properties, and there is no broad consensus on a set of signal features that strongly correlate with pore formation phenomenon during the LPB-F process. Researchers have investigated the sensor signal features corresponding to time, frequency, and time-frequency domains. Descriptive statistics operations from time waveform signals (e.g., mean, skewness, kurtosis, distribution) have shown success in identifying process lack of fusion, keyhole, and

balling regimes [34, 47]. Frequency and time-frequency domain spectral analysis features, recovered via Fast Fourier Transform (FFT) and Wavelet Transform (WT) analysis, have demonstrated the capacity for categorizing part density quality and detecting build flaws [48, 49].

This paper presents an approach to obtain high temporal resolution pore detection in L-PBF by merging and fusing information from multiple sensor modalities, including a microphone and two photodiodes in coaxial and off-axis configuration. The advantage of this approach is the integration and comparison of such low-fidelity sensors, which are characterized by their affordability, scalability, and ease of implementation. Additionally, each individual sensor has been assessed independently for detecting pore formation in the past. The proposed ML framework takes featurized and fused sensor data as input, and the output is the predicted labels signifying existence or lack of keyhole pores. Our objective was to develop an interpretable ML approach and explore the effectiveness of various sensor modalities. This was accomplished by utilizing two different signal featurization approaches, which allowed us to recognize hidden physical information carried by time-domain signals and gain insight into the relationship between defect creation and signal properties. These featurization approaches were applied to data collected during synchrotron imaging on single track experiments, in which pore formation times are unambiguously identified by the synchrotron imaging data. The results illustrate promising routes towards real time defect detection in L-PBF, with potential pathways for application in part-scale settings.

2. Methods

2.1 In situ X-ray Imaging of the L-PBF Process

Single-track laser irradiations and correlative diagnostic measurements were performed at the Stanford Synchrotron Radiation Lightsource (SSRL) using a test bed shown in Figure 1. The L-PBF system utilized a 1,070 nm, continuous wave, 500 W maximum power Yb-fiber laser (YLR-500-AC-Y14, IPG Photonics) focused to a spot size of approximately 73 μm in diameter (D4σ) for all experiments. The vacuum chamber containing the sample was evacuated to ~ $5x10^{-2}$ Torr prior to being filled with 730 Torr argon inert gas environment for processing. Argon was constantly flowed through the vacuum chamber during experiments at 500 SCCM, with the argon expelled into the chamber from a high-efficiency air knife (Super Air Knife, Aluminum, 3 in, EXAIR) located above the substrate surface. The argon flow was anti-parallel to the scan direction, such that the laser was scanning towards the argon source. During processing, the laser was scanned across a Ti-6Al-4V substrate (TMS Titanium, Poway, CA, USA) as a 2.5 mm long single line. The laser power was adjusted in 50 W increments, ranging from 50-400 W, while the scan speed was varied between 250-1250 mm/s at 250 mm/s increments. Each substrate was approximately 500 μm thick in the X-ray probe direction. Experiments were performed without powder on the surface to simplify experimental setup, as previous reports have illustrated that the presence or absence of powder slightly shifts the energy density of process regime thresholds but does not make important changes to underlying melt pool physics [50]. Full details of the experimental setup can be found in our previous work [44].

In situ X-ray imaging was performed at SSRL beamline 2-2 using an unfiltered polychromatic X-ray beam produced by a 1.25 T bend magnet with a critical X-ray energy of 7.4 keV [51]. Transmission X-ray images of the L-PBF process were captured using the scintillator-based optical

system, described by Martin et al. [44], operating at 20 kfps and 45 µs exposure time. This produced images with an effective pixel size of 2 µm, providing ~2×1.3 mm^2 field of view.

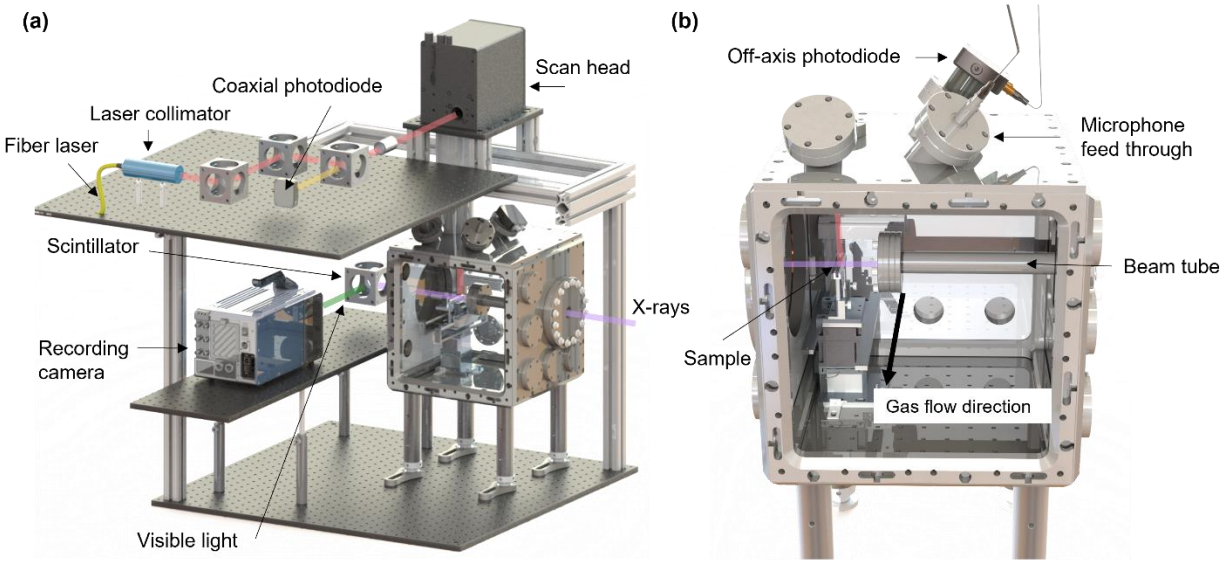

Figure 1 L-PBF test bed design details. (a) A computer aided design (CAD) rendering illustrating the laser optical pathway, coaxial photodiode configuration, processing chamber, and X-ray imaging system layout. (b) Rendering of a chamber close-up view demonstrating internal components and the placement of the off-axis sensors. The microphone is mounted to the inner surface of the flange, not visible in this view.

Three in situ sensors were used in these experiments. An off-axis photodiode (DET10A2, Si Detector, 200 - 1100 nm, 1 ns Rise Time, Thorlabs) was mounted on an optical window to provide line-of-sight to the substrate at a working distance of 340 mm and an offset angle of 34° relative to the substrate surface normal. A 1064 nm notch filter (86-128, Edmund Optics) was placed in front of the photodiode to remove contributions from the process laser scattered from the surface. The photodiode was connected to a low noise current amplifier with 10^6 gain setting and 10 µs rise time (428, Keithley). A photodiode was also installed in a coaxial configuration relative to the laser. The coaxial photodiode (DET10A2, Si Detector, 200 - 1100 nm, 1 ns Rise Time, Thorlabs) observes optical emission coincident with the laser at the sample surface by picking off the sub-950 nm optical emissions using a short pass dichroic mirror in the laser optical path. A 1064 nm notch filter (86-128, Edmund Optics) was placed in front of the photodiode to remove contributions from the process laser scattered or reflected from the surface. The field of view observed by the coaxial photodiode is always coincident with the process laser because it is defined by the same scan mirrors used for laser steering. The photodiode collection area corresponds to an approximately Gaussian cross section with D4σ = ~720 µm centered at the same location as the process laser spot. The collection area was determined by placing a white light source at the photodiode location, with the photodiode removed from the optical path. The diameter of the light source was defined by the 200 µm pinhole that is typically placed in front of the photodiode sensor to reduce the field of view. The back-propagated light from the photodiode location through the optical pathway was imaged in the sample plane using an optical camera. The measured profile of the back-propagated light corresponds to the photodiode measurement area. The photodiode was connected to a low noise current amplifier with 10^6 gain setting and 0.438 µs rise time (5402,

Ametek). A microphone was mounted in the chamber with direct line-of-sight to the laser-sample coincident plane at 44° offset angle and a working distance of 140 mm. The 1/4" free-field, prepolarized microphone and preamplifier package (Frequency Range: 4 to 100000 Hz (+2 / -3dB), dynamic range: 165 dB, 378C01, PCB Piezotronics Inc.) was mounted to the chamber using a BNC feedthrough vacuum flange. The microphone package was connected to a sensor signal conditioner (482C05, PCB Piezotronics Inc.) and the signal was then further conditioned using a voltage preamplifier (SR560, Stanford Research Systems). Synchronization of the laser scanning system, diagnostic sensors and X-ray imaging system was realized using a custom field-programmable gate array (FPGA)-based timing circuit (USB-7856, NI). All sensor signals were recorded as a function of voltage synchronously at 400 kHz using a FPGA-based laser interface module.

2.2 Signal Segmentation

The single-track experiments melted 2.5 mm of the Ti-6Al-4V substrate with a scan speed in the range of 250 to 1250 mm/s. Therefore, the total collection time of the sensor signals associated with each track varied approximately between 2-10 ms. The high-speed X-ray data collection at 20 kHz frame rate enabled the determination of pore formation time with an accuracy of ± 50 µs, allowing for temporal registration of the pore formation occurrences to segments shorter than the entire track lengths. To determine how the time scale of data collection of emitted signals affects the prediction of pore formation, signal partitions of 800, 400 and 200 data points, all collected at 400 kHz were explored. These segments correspond to 2.0, 1.0, and 0.5 ms windows in time. The prediction of pore formation events at time-partitions below 2 ms had not been investigated until recently [45]. This is mainly attributed to the challenges involved in extracting signatures from a sparse signal and short-scale pore formation registration. Labeling of the signal partitions entailed assigning class "1" to partitions with at least one pore and class "0" to pore-free segments. It is essential to note that labeling of pore-forming segments based on in situ X-ray images allows accounting for temporary keyhole pores that do not persist and are absorbed by vapor depression before being trapped by the solidification front, an advantage that ex situ registration techniques do not offer.

An example of signal segmentation, temporal registration of the synchronized X-ray images to monitoring signals and annotating partitions of a 4 ms track are shown in Figure 2. These images are time difference images, within which darker regions correspond to reduced X-ray absorption, while lighter regions indicated enhanced X-ray absorption. Image processing was conducted using a custom script developed in Mathematica, following a procedure similar to that described by Martin et al. [17]. This procedure generates time difference images, where each frame is divided by the uncorrected initial frame using the equation, $image = \ln(t_n) / \ln(t_0)$, where t_n and t_0 denote the intensity of a particular frame and the intensity of the initial frame, respectively.

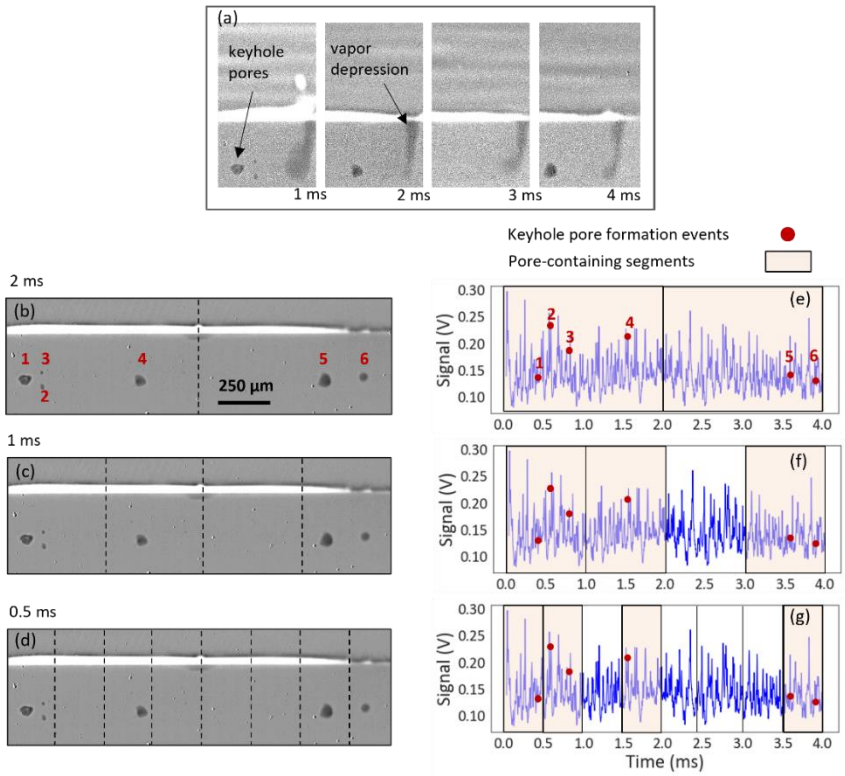

Figure 2. An example of sensor signal segmentation and registration to pore formation events. (a) Side-on X-ray images at four equal intervals during a 4 ms single-track experiment displaying the vapor depression region and the keyhole pores. Pore formation time is defined as the moment that the keyhole porosity is detached from the vapor depression, captured by an X-ray frame and marked by the red circles overlayed on sensor signals. The signal segment that includes at least one pore formation frame is assigned the class label "1". (b)-(g) Partitioning and temporal registration of the 4 ms track into three segment sizes of 2, 1, and 0.5 ms and elaborating the labeling strategy.

2.3 Signal Featurization

2.3.1 Power Spectral Density Featurization

In the first approach, we derived frequency-based features and exploited spectral signatures by estimating the Power Spectral Density (PSD) of the signal segments. The use of frequency information of the acoustic signal for process monitoring and defect prediction has been demonstrated previously [31-33]. Moreover, the existence of a periodic oscillatory response of the melt pool depression prior to pore formation turbulences has been shown in the literature [7].

PSD describes the distribution of the power of a time series across its frequency components. The computation of PSD is desirable when random effects in the signal may obscure the salient underlying patterns, while one can compute Fourier Transform for deterministic signals with minimal noise and randomness [52]. Periodogram-based estimation of PSD is a nonparametric method and involves computing the squared magnitude of the signal's Discrete-time Fourier Transform (DFT) [53, 54]. Welch's modified periodogram method is an improved estimator of PSD that has been used widely since it was introduced in 1967 [55]. It follows dividing data into L overlapping successive temporal intervals, calculating the periodogram of each partition and averaging them to obtain the PSD estimate at frequency ω , $S(\omega)$.

$$S(\omega) = \frac{1}{L}\sum_{l=1}^{L} P_l(\omega), \quad (1)$$

where $P_l(\omega) = \frac{1}{N}|X_l(\omega)|^2$ is the periodogram of l^{th} interval of size N. The DFT of the sequence $x[n]$ is denoted by $X_l(\omega)$ and is equal to $\sum_{n=0}^{N-1} x[n] \exp(-j2\pi\omega n)$.

A smaller interval size results in obtaining a smoother PSD estimate since the random effect of noise is averaged out. However, this outcome is achieved at the expense of compromising the frequency resolution (frequency resolution = sampling frequency/interval size). In this work, the interval size was chosen according to the shortest signal segment with 200 data points (0.5 ms length in time) which produced 100 PSD features at a frequency resolution of 2 kHz. To ensure that the PSD features obtained from the three segments were comparable, the size of the interval was maintained at 200 data points throughout the study.

2.3.2 Highly Comparative Time Series Analysis (HCTSA) Featurization

In the second approach, featurization was expanded over a comprehensive bank of operations to capture a wide range of time series properties. Attributes such as basic statistics of the distribution, linear correlations, stationarity, entropy, frequency, and non-linear analysis measures were included in the feature bank by computing over 7000 distinct featurization operations. This was accomplished by using the highly comparative time series analysis (HCTSA) toolbox developed by Fulcher et al. [56]. The toolbox became publicly available in 2013 and has been used for signal processing studies in various disciplines [57-59] including L-PBF applications by Tempelman et al. [42].

Figure 3 presents the workflow we employed to derive HCTSA feature sets. The HCTSA feature banks were computed for the acoustic, off-axis, and coaxial photodiode measurements and subsequently were filtered down to ~ 5500 well-computed features for each modality (features returning error values were removed). Due to the large number of computed features, it is expected that feature multicollinearity will prevail, which may lead to challenges in developing reliable predictive models. The solution is to eliminate highly correlated and redundant features and only maintain ones carrying unique signal attributes. Feature pairs with absolute correlation coefficients greater than 0.8, were discarded. This removed approximately 3000 redundant features but the remaining ~2000 features were still computationally demanding, stressing the necessity for an informed downselection.

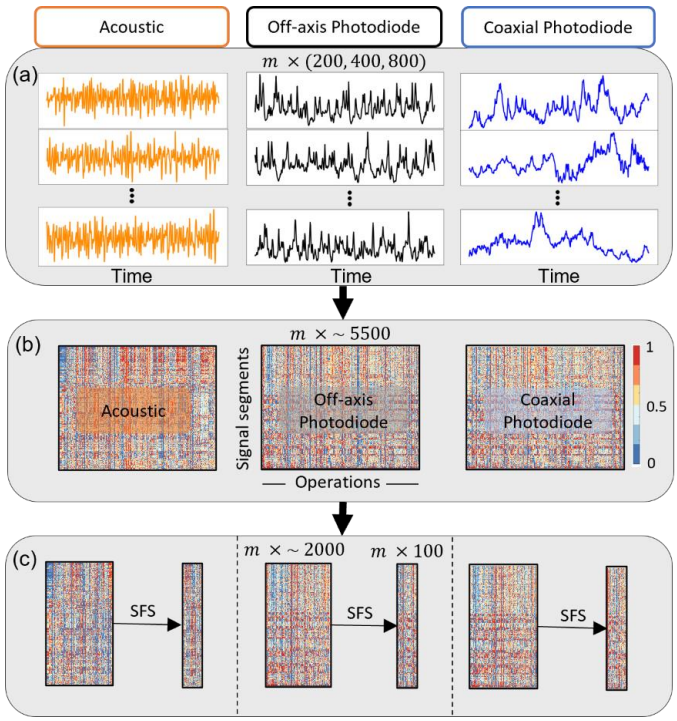

Figure 3. The workflow of the HCTSA featurization method. (a) The raw time series of the acoustic, off-axis, and coaxial photodiode sensors. The total number of the segmented signals, designated by *m*, is produced by dividing monitoring signals into 200, 400, and 800 size partitions. (b) The massive feature bank computed for each sensory modality using the HCTSA toolbox. The time series are plotted as rows and features as columns and the value of each feature on each time series is visualized using a colormap that maps the color spectrum from blue (0) to red (1), corresponding to the normalized feature values. (c) The feature size reduction strategy to minimize feature correlation and identify the top acoustic, off-axis, and coaxial photodiode features using the SFS routine.

To further downselect the remaining 2000 features, we employed the Sequential Feature Selection (SFS) strategy to search for the most relevant subset of features. SFS differs from the less computationally complex methods such as Recursive Feature Elimination (RFE), where the feature weight or importance coefficient is used to eliminate features recursively, whereas in SFS, selection is based upon a predetermined classifier algorithm and performance metric to discover the best performing feature subset [60]. SFS is divided into two categories, forward and backward selection. The former starts with an empty set and adds features while the latter starts with a full set and removes features one at a time. At each step, the choice of which feature to add or eliminate is governed by its effect on the model performance to raise it to its maximum value. An extension of SFS is sequential "floating" feature selection (SFFS) that was introduced to mitigate the so-called "nesting" effect [61-63]. In the original SFS strategy, once a feature is selected/discarded, it cannot be deselected/included later. The result is that the methods are suboptimal. In the floating version, after each executed forward selection step, it performs a backward selection to discard features in case this improves the feature set's performance evaluation metric. Correspondingly, the floating backward selection entails a forward selection after each backward step.

Here we used forward SFFS to discover the top 100 features for each signal modality that offered the best separability between the pore-affiliated and pore-free signal segments. To ease the associated computational burden of processing thousands of features, Linear Support Vector

Machine (L-SVM) algorithm was selected due to its memory efficiency and the performance evaluation metric of F1-score was used to assess model performance, which is defined later in Section 2.5.

2.4 Multimodal Data Fusion

In the data fusion hierarchy, information fusion can take place at the signal, feature, and decision levels. At the signal level, the raw time series partitions are combined prior to featurization. The feature level data fusion involves independent featurization of the signal modalities and fusing the extracted features. At the decision level, sensor-specific models are trained individually, and optimal combination of the decisions yields the outcome [64, 65].

In this work, we utilized feature-level fusion that returned a fused feature matrix ($\mathbb{X}$) of size $m \times 300$ (Figure 4), where m denotes the number of observations and is equal to 210, 484, and 1031 for 2, 1, and 0.5 ms signal partitions, respectively. Each row of $\mathbb{X}_{m\times300}$, is an ensemble of 100 acoustic, off-axis, and coaxial photodiode features corresponding to a single signal segment (x_i) that is paired with a class label (y_i) from column matrix $\mathcal{Y}_{m\times1}$. By adopting a naive approach and training the classifiers on a 300-dimensional fused feature vector model, overfitting may be an issue. Moreover, many features of the coaxial and off-axis photodiode signals are undoubtedly correlated. Hence, we implemented forward SFFS over $\mathcal{Z} = \{\mathbb{X}, \mathcal{Y}\}$ to uncover the most informative subset of fused features for differentiating porous and pore-free segments. The SFFS methodology determined the optimal feature sets for each classification algorithm that are outlined in the next section.

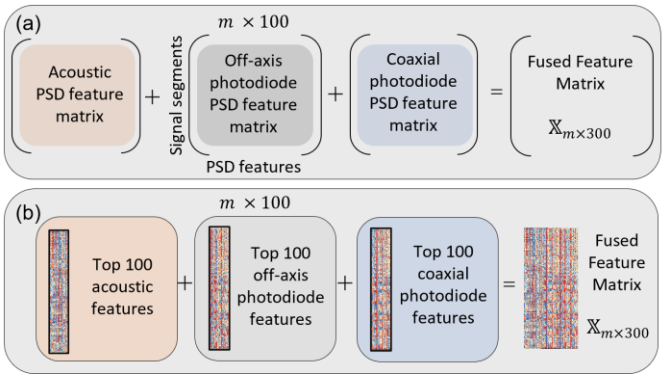

Figure 4. The feature level sensor fusion of (a) PSD and (b) HCTSA multimodal features to create fused feature matrices.

2.5 Classification Algorithms and Model Validation Strategies

In this study, three machine learning algorithms were implemented: Support Vector Machine (SVM), K-Nearest Neighbor (KNN), and Gaussian Naïve Bayes (GNB). SVM classifiers are among the most robust and widely used prediction algorithms to establish mapping between the in-process features and the class labels. As a discriminative method, SVM aims to find a hyperplane that separates data points of different classes by maximizing a margin, through an optimization problem. The decision boundary defined by this hyperplane is based on the maximum margin principle. One of the primacies of the SVM is its applicability to nonlinear problems through employing kernel functions [66]. KNN and GNB algorithms differ from the SVM

algorithm as they do not entail optimization of a cost function. KNN implements the concept of a majority voting mechanism. It identifies similarities between the test data and all the training points by calculating distances. The class that is most common among the *K* nearest neighbors of a single testing datapoint will be assigned to it [67]. In practice, there is no training involved in a KNN algorithm, which makes it expensive in real time as all the training data is utilized in the testing phase to find the neighboring nodes. Instead, the GNB algorithm has the superiority of efficient training. GNB is a generative probability model built based on the Bayes Theorem and performs well on small training sets. GNB implicitly assumes that all features follow the Gaussian distribution and are mutually independent, which can be disproved in real-world cases [68]. Nevertheless, it is a fast and simple algorithm that has turned it into a viable choice for real-time predictions.

The primary purpose of the model validation is to examine the generalization ability of the trained ML model for classifying unseen data. It is carried out through the cross-validation procedure using different performance metrics. The decisions for the proper performance metrics hinges on the type of the model and the application. Accuracy, recall, precision, and F1-score are commonly found to be useful measures for evaluating binary classifiers. These performance indicators are determined from the total number of True Positive (TP), True Negative (TN), False Positive (FP), and False Negative (FN) predictions. We treated pore-free segments as negative and pore-containing ones as positive predictions.

$$\text{Accuracy} = \frac{TN+TP}{TP+TN+FP+FN} \tag{2}$$

$$\text{Recall} = \frac{TP}{TP+FN} \quad , \quad \text{Precision} = \frac{TP}{TP+FP} \tag{3}$$

$$\text{F1} = 2 \times \frac{Precision \times Recall}{Precision+Recall} \tag{4}$$

Accuracy quantifies the model's ability in making correct predictions. What is often neglected is that accuracy metric falls short in assessment of imbalanced data sets, which is the case for the majority of the defect detection applications. The value of the accuracy metric can become misleadingly high by correctly predicting the dominant class (pore-free segments), even though the classifier does not excel at identifying defective features (minority class). To mitigate such risk, we centered our evaluations around F1-score, harmonic mean of recall and precision. In our application, recall quantifies the ratio of the porous segments that have been successfully identified by the model while precision measures the model's sensitivity to false positives. A low precision metric implies that a small ratio of the identified porous segments truly contains any pores. In this work, we gave stronger preference to models with higher recall if the obtained F1-scores were comparable.

The Repeated Stratified 5-fold cross validation used in this study splits data into 5 non-overlapping sets while the percentage of the samples for each class is preserved within the created folds. Each group is given the opportunity to be excluded from the training set and be used as the testing data. With 10 repetitions, 50 independent trials were performed that ensured the returned average values are representative of the model general performance.

3. Results and Discussions

Figure 5 displays the average vapor depression depth and laser energy density maps across the designed process window. At low laser power and scan speeds, no discernable vapor depression was detected. The onset of the keyhole pore appearance was observed to be at 150 W and persisted at all tested laser power increments. Figure 5 (b) shows that the process window with prevailing pore formation, exhibits the highest average vapor depression depth owing to the increased deposited laser energy density (Figure 5 (c)). Note that the defect severity is not uniform across the defect-prone region and is most pronounced at 250 mm/s, corresponding to the highest laser energy density. It is important to remark that at high laser powers and medium scanning speed (500 mm/s), which are associated with significant vapor depression depths, no drastic defect generation is observed, mainly due to the diminished energy density. Lastly, beyond 500 mm/s, the pore formation propensity declined considerably with reduction of the coupled vapor depression depth and deposited energy level.

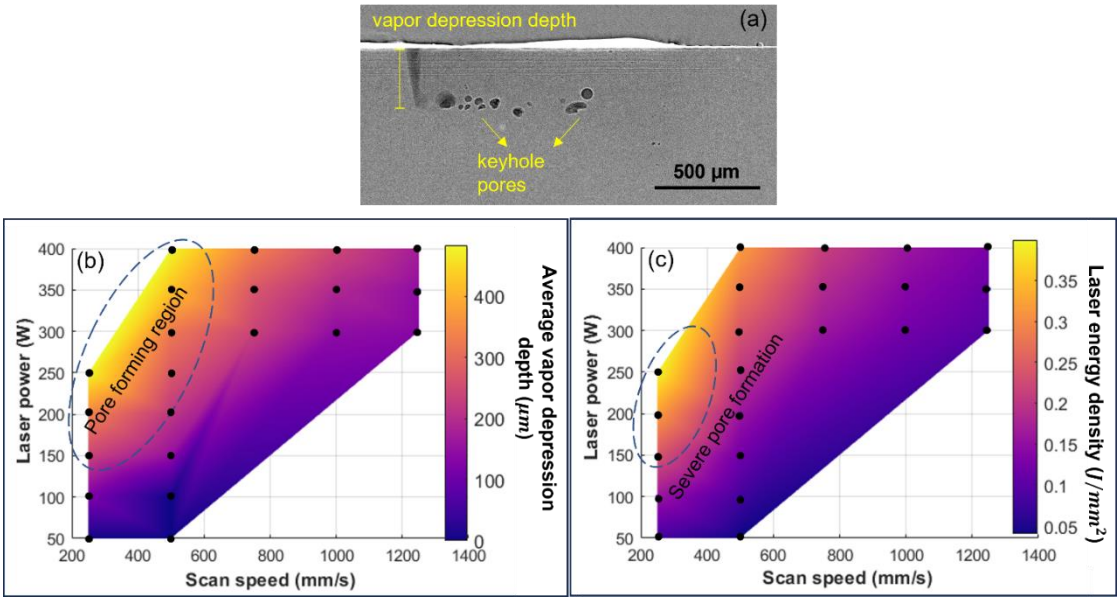

Figure 5. (a) A side-on X-ray image of a Ti-6Al-4V substrate, depicting subsurface keyhole pores and vapor depression region during laser scan at 250 W and 500 mm/s. (b) The average vapor depth of penetration and (c) the laser energy density surface plots for the given process window, which were derived by extrapolating the measured datapoints shown by dots.

Table 1 details the total number of pore-containing and pore-free signal segments obtained after partitioning the process monitoring signals from the entire process window depicted in Figure 5. By creating shorter time series segments, the pore-free class becomes dominant, establishing the class ratio of 0.44 for 0.5 ms segments. This ratio is defined as the total number of pore-containing segments over pore-free ones ($N_{(pore)}/N_{(no\_pore)}$). Deviation of this value from unity signifies skewed class proportion.

Table 1. Summary of the binary datasets created from monitoring time series using different segment lengths.

Segment length	Sample size	Class ratio

2 ms (800 pts)	210	1.26
1 ms (400 pts)	484	0.77
0.5 ms (200 pts)	1031	0.44

Figure 6 reports an example of the PSD estimates of the three sensor signals (acoustic, off-axis, and coaxial photodiode), computed for two consecutive signal segments. The X-ray image in Figure 6 (a), illustrates the spatial locations on the Ti-6Al-4V substrate. The first and the second dashed squares outline a pore-encouraging and a pore-suppressing segments, respectively. The unique characteristics of each sensor modality data is evident from their raw time series signals, shown in Figure 6 (e-j). Acoustic time series exhibits pronounced oscillations in amplitude and frequency, developing PSD peaks greater than 40 kHz. Whereas the reduced fluctuations of the thermal emission signals, particularly coaxial photodiode, have led to PSD peaks emerging at significantly lower frequencies and magnitudes.

Examination of the PSD features (Figure 6 (b-d)) reveals differences in the responses of the monitoring signals upon pore formation, showcasing the sensitivity of the sensor signals and the PSD features to the changes in process dynamics. These changes are particularly more pronounced for the acoustic signal (Figure 6 (b)), with the emergence of peaks below 40 kHz, which is consistent with the observations of keyhole fluctuations in previous studies [7, 45]. Both photodiode signals exhibit dominant low-frequency oscillations that weaken in the porous region. While Figure 6 (d) shows no other notable distinction between the “pore” and “no-pore” signals of the coaxial photodiode, an emergence of minor peaks in the off-axis signal at the vicinity of 40 kHz is evident from Figure 6 (c).

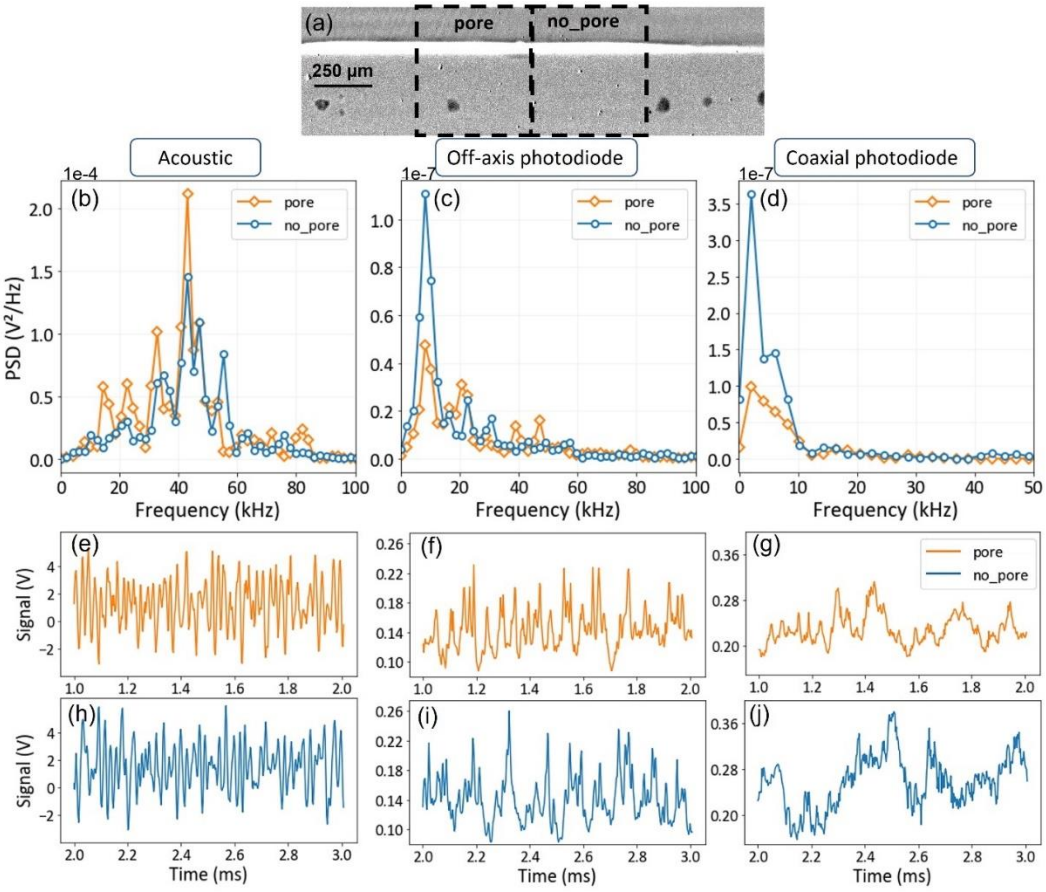

Figure 6. An example of PSD featurization implemented on the acoustic, off-axis photodiode, and coaxial photodiode signals of a pore-containing and pore-free segments. (a) X-ray image illustrating two consecutive segments on a Ti-6Al-4V plate with and without any keyhole pores. (b-d) PSD features of the "pore" and "no-pore" segments for each sensor modality. The plots comprised of 100 power spectral density values with the resolution of 2 kHz, spanning the frequency space of 0-200 kHz. However, to facilitate a better visualization of the lower-level fluctuations, higher frequencies are truncated if the curve has reached a plateau. (e-j) The corresponding raw time series.

The results in Figure 6 only display the PSD features for a single example. To develop a more comprehensive insight into the impact of porosity generation on the PSD features of the monitoring signals, the PSD peaks for the pore-containing and pore-free segments were extracted for all signal segments by identifying the local maxima of the plots. Figure 7 demonstrates the normalized histograms of the peak frequencies for all signal segments, accompanied by the corresponding probability density function (PDF) of Weibull fits. The Weibull fit is highly versatile in accommodating a wide range of distributions. It is characterized by two parameters: the shape (κ) and scale (λ) factors. The shape parameter reflects the skewness or symmetry of the distribution. When κ<1, the highest probability density is achieved for the lowest frequencies (Figure 7 (c)). As κ becomes greater than one, the distribution transforms into a right-skewed bell shape, similar to Figure 7 (a-b). With further increase the distribution gradually transforms into a normal and then left-skewed bell shape distribution. Additionally, the scale parameter provides information about the typical or average value around which the data is centered and it corresponds to the 63.2 percentile of the distribution [69].

The plots of Figure 7 illustrate that each sensor exhibits a unique frequency distribution and shape factor. The scale factor (λ) of the pore-forming regions is around 45 kHz for all the three signal sources. The off-axis photodiode and the acoustic sensors have captured a clear distinction between the "pore" and "no-pore" frequencies while the most prominent difference in the coaxial photodiode distributions is the reduced oscillations of the defective segments at around 5 kHz. In plots of Figure 7 (a-b), the scale factor of the pore-containing regions has decreased which indicates less dispersed fluctuations and a greater likelihood of the peak oscillations is expected. The periodic oscillations of the keyhole's morphology have been previously identified as a precursor of chaotic turbulence, which can lead to pore formation [7]. These oscillations result from a periodic widening and necking of the keyhole opening, due to repetitive overheating and cooling at a frequency of approximately 40 kHz, that are induced by competing forces of surface tension and recoil pressure. This behavior transitions to a multimodal regime that generates persisting keyhole pores. We hypothesize that the acoustic signals observed in this work arise from mechanisms related to oscillatory keyhole dynamics that lead to fluctuations in the melt pool, which in turn generate pressure waves in the Ar cover gas by modulating the vapor plume generation. However, the X-ray imaging data reported here cannot resolve melt pool fluctuations at these timescales so this hypothesis cannot be directly confirmed with this dataset. Note that frequencies above 100 kHz are beyond the frequency response range of the implemented microphone, and therefore the observed acoustic fluctuations greater than 100 kHz are electronic noise and are not attributed to actual acoustic signals. Moreover, from the analysis of the background signals recorded by the photodiode sensors, it was found that the frequencies above 100 kHz are predominantly induced by environmental noise rather than signal originating from the process of interest.

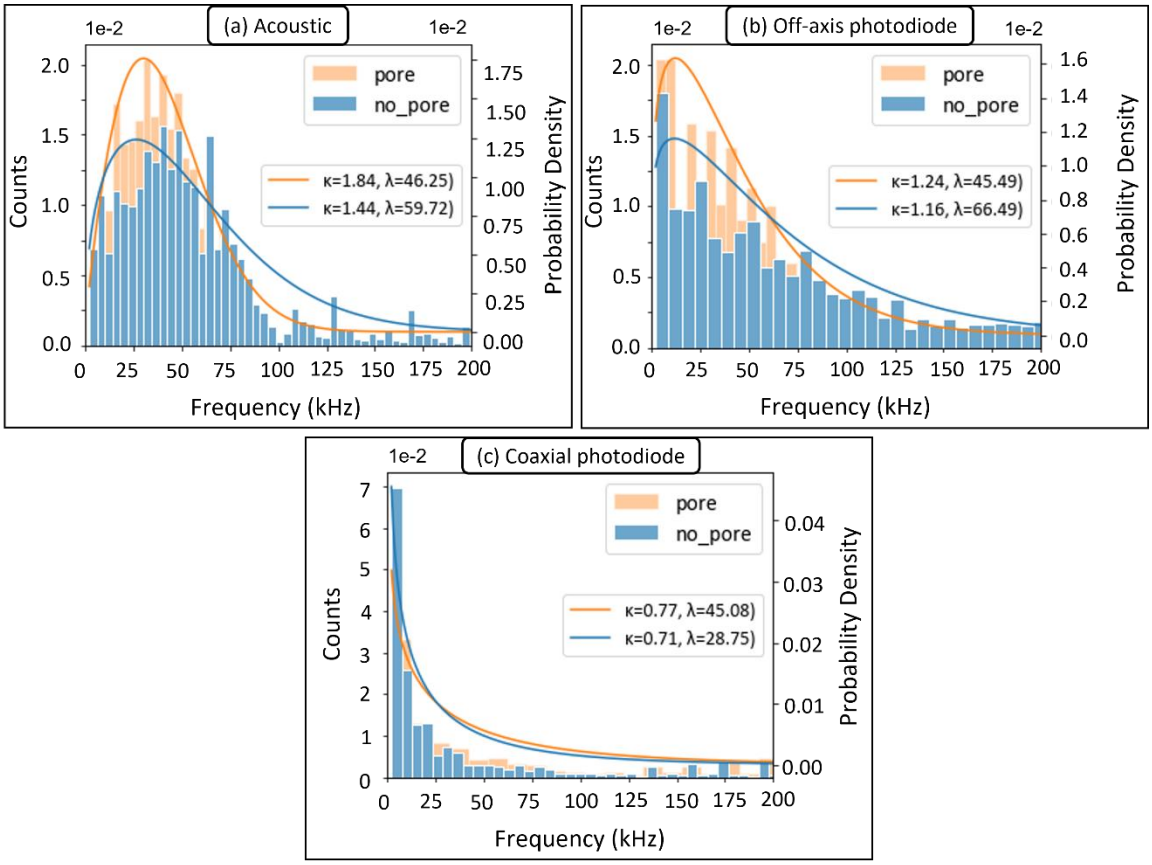

Figure 7. Probability density function curves of the PSD peaks determined by identifying local maxima of the corresponding PSD curves for (a) acoustic, (b) off-axis photodiode, and (c) coaxial photodiode sensor signals.

The top 100 HCTSA features were determined for each sensor signal using the workflow presented in Figure 3. The fused feature matrices ($\mathbb{X}_{m\times 300}$) of dimensions 210×300, 484×300, and 1031×300 were delivered for both the PSD and HCTSA featurization techniques by aggregating the multimodal feature banks. In comparison to PSD, computation time of the HCTSA features was substantially more expensive and orders of magnitude higher. HCTSA requires several hours (up to 10 hours for a sample size of 1031) whereas PSD features are computed in a matter of seconds using an Intel(R) Xeon(R) Silver 4214R CPU 2.4 GHz processor with 128.0 GB of random-access memory (RAM). This is partly due to the larger number of HCTSA features (100 PSD versus over 7000 HCTSA features).

For each respective classifier, our feature selection scheme, SFFS, recovered the optimal feature set independently according to their impact on improving the model performance. To avoid overfitting, small feature spaces were preferred if different feature sets yielded comparable results. The radial basis function (RBF) kernel was employed for the SVM models. In addition, the computation of the distance to the nearest neighbors in the KNN models were based on Euclidean distance metric. A naive grid search technique was used to optimize the KNN and GNB model hyperparameters and the values of the tuned hyperparameters are provided in Appendix A. A few examples of the SFFS results are presented in Figure 8. The plots illustrate the 5-fold cross validation estimates of the F1-score for the SVM, KNN, and GNB classifiers trained on the

HCTSA fused feature matrix of 2 ms signal segments. SFFS identified a subset of size 14, 15, and 20 features, respectively, that resulted in the maximal performance. The subset of 15 features was selected for the KNN model even though the actual peak is at 45. The substantial smaller number of features ensured model generalizability which is favored over minor performance enhancement. Furthermore, the adverse impact of increasing feature size shown in Figure 8 affirms the necessity for the adoption of informed feature selection scheme on fused feature banks to circumvent multicollinearity and model overtraining. The comparable or reduced performance beyond the optimal set certifies that the relevant information has already been captured and addition of more features contribute to information redundancy. The complete list of the number of selected PSD and HCTSA features for each model can be found in Appendix A.

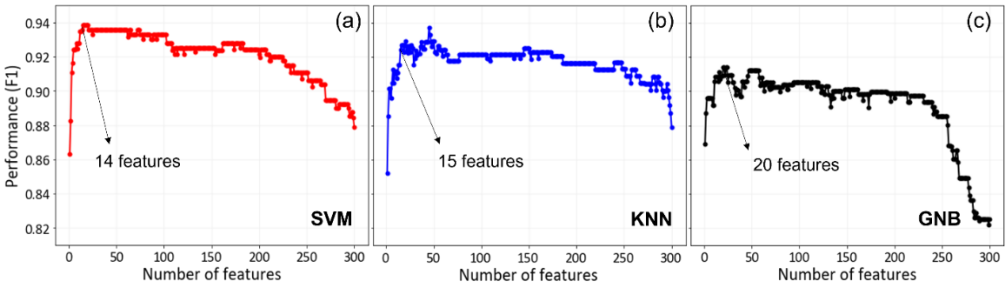

Figure 8. An example of forward SFFS results applied on the 2 ms HCTSA fused feature bank. A unique feature set is selected for each classifier. The performance jumps rapidly with the first few feature additions and once it reaches the maximal score, the gradual reduction is observed in all three cases. The incorporation of the full feature set provides one of the lowest scores.

The classification performance of the three classifiers for each featurization strategy and signal size is presented in Figure 9. The distribution of the F1-score over 50 independent cross-validation trials is given in Figure 9 (a) and the corresponding average accuracy and recall values are shown in Figure 9 (b-c). It is evident that regardless of the feature type, the performance has improved with the signal segment size, as has been observed in other studies [42, 45]. This can be further elaborated by probing the impact of segment size on the derived PSD values (Figure 10). According to Equation (1), given that all PSD curves are calculated using the same interval size (N), the distinction between the results of different segment sizes originates from the varying number of their overlapping partitions (L). Increasing the signal segment size and subsequently the L value results in assigning signal power more accurately to the correct frequencies. Moreover, the noise-induced fluctuations in the signal power amplitude that can be seen in the 0.5 ms curve of Figure 10, are discernably reduced by increasing the segment size that yields a smoother PSD curve. Thus, the larger signal segments capture process signatures more effectively and are a better representative of the signal behavior. These performance benefits from increasing the segment size are gained at the expense of lowering the temporal resolution of the model predictions.

Note that, the impact of temporal resolution on the three presented measures (F1-score, accuracy, and recall) is not similar. The recall measure demonstrates lower susceptibility to the segment size. Figure 9 (c) shows that the recall score of the HCTSA-SVM model is subjected to only 8% reduction, from 0.97 ± 0.03 for the 2 ms model to 0.89 ± 0.04 for the 0.5 ms model, while achieving finer time resolution by a factor of 4. This reflects the model's ability to detect an average of 89%

of pore formation events at 0.5 ms time resolution. In such cases, the precision-recall trade-off leads to higher rate of false positives, manifested through the associated lower F1-score at 0.5 ms. Interestingly, closer examination of the models reveals that lowering the signal length from 1 ms to 0.5 ms diminishes performance more severely than 2 ms to 1 ms reduction.

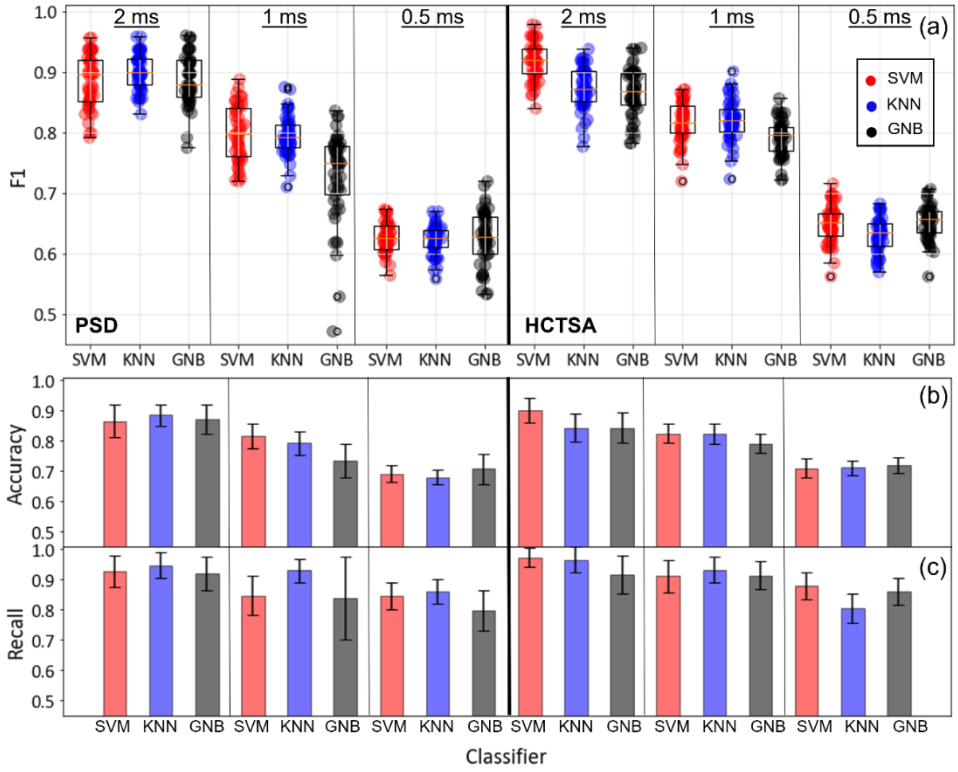

Figure 9. Classification performance of the eighteen models to explore the effects of signal segment size, featurization approach, and classifying algorithms. (a) The distribution of F1-score, the primary evaluation metric, over 50 cross-validation trials. (b-c) The bar plot of the corresponding average accuracy and recall measures.

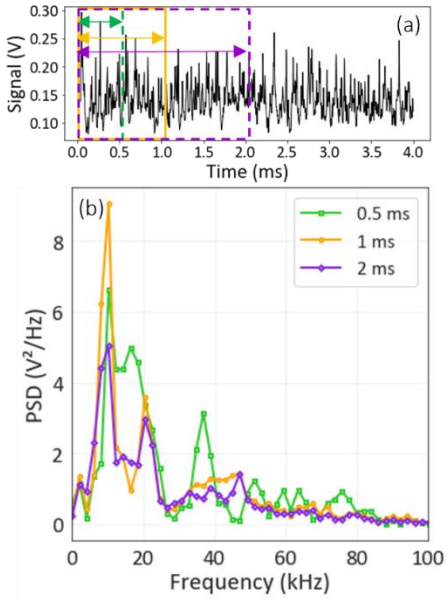

Figure 10. An example of PSD derivation from an off-axis photodiode signal of different lengths to highlight the impact of the signal segment size. (a) A raw time series displaying 2, 1, and 0.5 ms signal partitions. (b) The corresponding PSD features of the shown signal segments. This plot only displays frequencies up to 100 kHz, as higher frequencies exhibited a plateau at 0 V^2/Hz.

The results of Figure 9 corroborate that the effect of the classifying algorithm is minimal in most cases. GNB algorithm predominantly offered higher variance in the cross-validation results, particularly with PSD features and 1 ms segment size. As was mentioned earlier, the best performing models were selected based on their F1-score, and if two models offered the same score, their recall values were inspected. At 2 ms, the SVM algorithm showed superiority among the other HCTSA models, with respect to all the three F1-score, accuracy, and recall measures. The similar comparison for the PSD models showed the outperformance of the KNN algorithm by a small margin. Even though SVM and KNN performed comparably at 1 ms, KNN became a more suitable choice due to its slightly higher recall value. Analogously, at 0.5 ms, SVM classifier prevailed. The most likely explanation for the poor performance of the GNB algorithm is the falsification of its two fundamental assumptions: independence between features given the class label, and that the data is well-modeled by Gaussian distributions. It is likely that the coaxial and off-axis photodiode signals possess a degree of correlation, and all three modalities deviate from a pure Gaussian distribution. On the other hand, it is important to recognize that despite the comparable efficacy of the SVM and KNN models, the high computational time of KNN, makes it a less viable choice in practice if processing large datasets or real-time decision making is intended. Given the described selection criteria the results of the best performing PSD and HCTSA models are presented in Table 2.

Table 2. Performance summary of the top PSD and HCTSA models for the three segment lengths, with standard deviation from cross-validation noted (2 ms, 1 ms, and 0.5 ms).

	HCTSA models			PSD models		
	F1-score	Recall	Accuracy	F1-score	Recall	Accuracy

2 ms	0.92±0.03	0.97±0.03	0.90±0.04	0.90±0.03	0.95±0.04	0.88±0.03
1 ms	0.82±0.03	0.92±0.04	0.82±0.03	0.80±0.03	0.93±0.04	0.79±0.04
0.5 ms	0.65±0.03	0.89±0.04	0.70±0.03	0.63±0.02	0.85±0.04	0.70±0.03

Table 2 shows that an average of 2.0%, 2.3%, and 1.7% higher F1, recall, and accuracy is achieved from the HCTSA models. Such differences are within the performance variance range calculated for each model. Thus, the outperformance of the HCTSA models is not salient and the featurization approaches establish similarly performing models. However, the information carried by the corresponding features of each PSD and HCTSA models are fundamentally distinct. To interpret physical mechanisms underlying important features, it is imperative to understand how strongly each sensor signal has contributed to the best performing data fusion models.

To do this, we explored which sensor carries the most relevant information to the pore creation phenomenon. To quantify signal modality contribution to performance of the models in Table 2, we employed feature importance score, which is a common way to develop interpretable ML models. The permutation feature importance method is expressed to be the "decrease" in a model performance when a feature value is randomly shuffled while other features are kept intact [70]. The performance with the permuted feature value is compared to baseline performance with the original feature value. Higher reduction in performance, measured by the F1-score in this study, indicates how strongly the model predictions rely on the target feature. The bar plots of Figure 11, represent the average scores for the multimodal features, obtained from 20 repetitions, providing a robust estimate of the feature importance.

Figure 11 provides insight into two sets of information, the total number of features selected from each sensor source and importance score of each individual feature. The influence of the featurization approach (i.e., PSD and HCTSA) on the significance level of the three signal sources is clearly observed, which aligns with the expectations considering the distinct signal information they entail. It is intriguing that, even though acoustic signal holds a small share of the total feature space in the PSD models, those features hold the highest level of significance (Figure 11 (a-c)).This indicates that the information carried by the acoustic spectra, particularly at around 30-35 kHz, is highly related to the keyhole pore formation. Another interesting observation in Figure 11 (a-c) is the higher score of the off-axis photodiode in comparison with the coaxial photodiode features. Given that the coaxial sensor monitors only a small area in the immediate vicinity of the melt pool, the higher significance of the off-axis photodiode sensor, which monitors emitted light throughout the entire build chamber, suggests that thermal emission signatures related to keyhole pore formation are not restricted to the laser incident area and could be emitted from other regions of the melt pool. We hypothesize that this could be attributed to hot spatter events, emission from the plume, or fluctuations in the region of the melt pool far from the keyhole. Furthermore, the difference in the angle of observation in a coaxial and off-axis configuration can result in notable distinction in the captured emissions. The coaxial sensor monitors the keyhole depth while the off-axis photodiode observes the upper wall of the keyhole, close to the surface. In addition,

irrespective of the signal segment size, the off-axis photodiode shows the most noteworthy correlation with pore formation phenomenon in the vicinity of 30-35 kHz fluctuations.

Our observations from the PSD models based on spectral analysis, are consistent with other studies that report more reliable measurements by off-axis thermal setups than coaxial and achieving lower prediction efficiency when using pyrometry signals compared to the acoustic emission [42, 45]. We hypothesize that the origin of the acoustic signatures stimulated by pore generation can be partly ascribed to disturbances introduced to the vapor plume and surface melt pool oscillations. The periodic oscillation of the keyhole opening results in fluctuations in the plume intensity and strength, which, in turn can have an impact on acoustic emissions. Further experimental investigation is required to confirm the specific mechanism causing the difference in importance due to photodiode collection geometry as well as the mechanisms responsible for acoustic emission signals.

The feature importance results of the HCTSA models, shown in Figure 11 (d-f), demonstrates that even though the feature space of the models is primarily dominated by the acoustic source, the contribution of thermal emission features is substantial in terms of both the number of features and their impact. This is particularly discernible in the "HCTSA-1 ms" model, where the off-axis photodiode feature set outnumbers the other two signal sources and yields substantially higher importance scores compared to the off-axis photodiode features of the 2 ms and 0.5 ms HCTSA models. Figure 11 suggests that the contribution of each modality to the accuracy of model predictions varies depending on factors such as the signal time scale and the approach used for feature extraction. It appears that HCTSA features capture certain aspects of the thermal emission signals that are not present in the PSD features, which are associated with pore generation events.

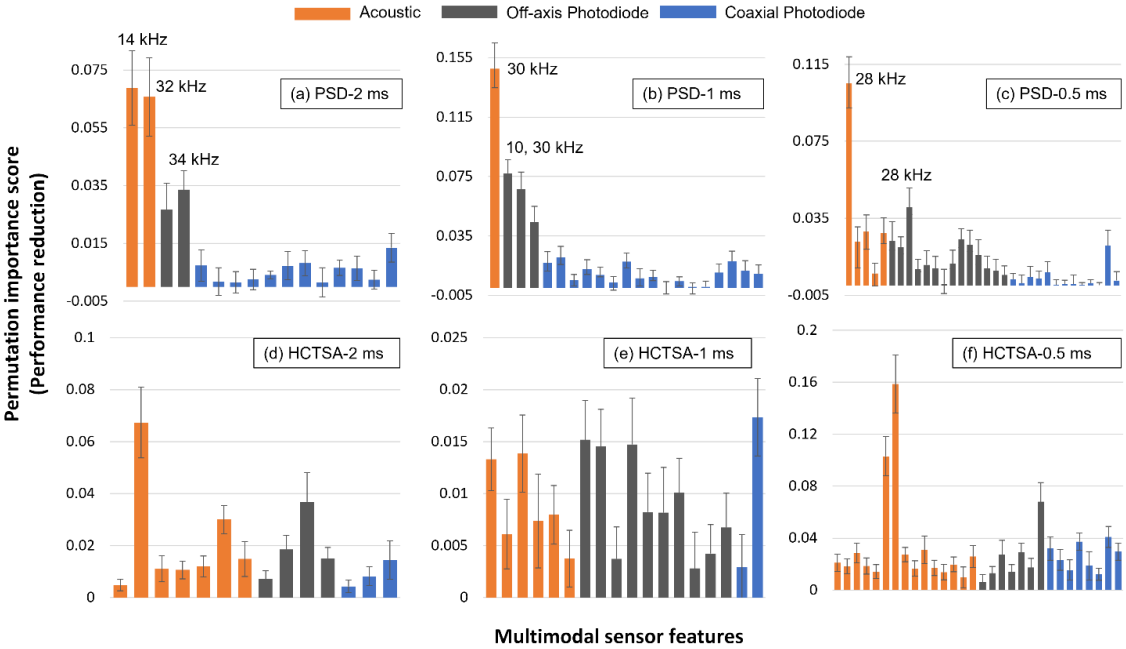

Figure 11. Model specific feature analysis results to demonstrate the contribution of the different signal sources and their corresponding features to performance of (a-c) PSD and (d-f) HCTSA models.

To identify the signal properties that are conveyed by the top HCTSA features, we implemented the `TS_TopFeatures()` function provided by the HCTSA package that delivers the most discriminative features. Figure 12 presents the distribution of two of the top acoustic, off-axis, and coaxial photodiode features. Note that the feature values are normalized between 0 and 1. The complete list of top-ranked features from each sensor modality are detailed in Appendix B. The features of acoustic measurements largely embody the information on the amount of uncertainty and randomness in the signal. In addition to the simple statistical measures such as signal standard deviation, more complex properties including signal entropy can express such characteristics and are shown in Figure 12 (a-b). It is evident that both features have captured the unique behavior of the pore-free and pore-containing signals. The low entropy values of the porous regions (Figure 12 (b)) reflects that the corresponding acoustic signals are less random, and signals consist of repeated patterns. In other words, the distribution of the frequencies in the signal is not evenly spread, but instead is dominated by a few specific frequencies, which is consistent with the observations of Figure 7 and Figure 11 (a-c). The combination of this characteristic with the higher standard deviation observed in Figure 12 (a), suggests that creation of the keyhole pores results in the amplitude of the acoustic fluctuations to vary substantially. The keyhole regime is known for its dynamic and complex attributes. Our findings indicate that amidst the chaotic response of this regime, a discernible non-random oscillation arises at short time scales, ultimately leading to pore generation. This observation aligns with prior research that have identified two keyhole modes, only one of which prompts porosity formation, and is defined by fundamental periodic oscillations [7, 45].

The top off-axis photodiode feature distributions, presented in Figure 12 (c-d), provide information about the signal's stability, evolution over time, as well as its level of randomness. The pore-containing segments of the photodiode signals exhibit a significantly higher convergence rate, Figure 12 (c). A high convergence rate indicates that the signal undergoes rapid changes and quickly returns to its previous state, implying that the disruptions in the signal attributes due to pore formation occur at short time scales and the signal converges to the pore-free state rapidly. On the other hand, the "no-pore" regions, which are free from defects and abnormalities, display a lower convergence rate, which suggests that these segments maintain a more stable and consistent behavior over time. Additionally, the porous regions show lower entropy compared to the pore-free signals, indicating a reduced level of signal randomness analogous to the acoustic signal source.

Finally, even the coaxial photodiode signals that are less effective in capturing keyhole signatures were found to show distinctive properties once keyhole pores were generated. In Figure 12 (e), the distribution of residual sum of square (SSE) is presented for polynomial fits to the cumulative PSD curves of the coaxial photodiode signals. The SSE values are noticeably lower for the pore-forming class, indicating that a polynomial model can more accurately represent the shape of the PSD curve for pore-forming regions. The implication is that the frequency content of the signal from pore-forming keyhole regions is more predictable compared to no-pore keyhole regions. The feature distribution displayed in Figure 12 (f) quantifies stationarity of the signal. The pore-forming signal

segments exhibit higher non-stationary characteristics. This means that the properties of the signal such as mean, variance, and autocorrelation are dynamic and tend to vary over time.

In general, it is apparent that there is a commonality in the type of information conveyed by these features, and through the use of more complex signal processing algorithms, HCTSA is able capture a broad spectrum of time series characteristics that differentiate between the segments of the monitoring modalities containing keyhole pores and those that are pore-free.

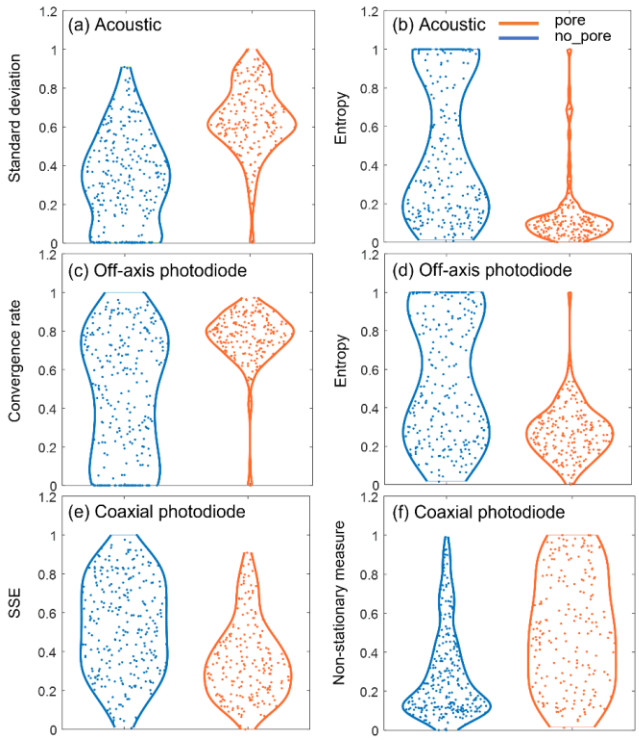

Figure 12. Distribution of the top HCTSA (a-b) acoustic, (c-d) off-axis photodiode, and (e-f) coaxial photodiode features, depicting diverse signal properties. Each plot represents a characteristic that distinguishes between the pore-free and pore-forming segments.

4. Conclusion

This study utilized high-speed synchrotron X-ray imaging and multimodal monitoring sensors to identify and predict keyhole pore formation in the L-PBF process. Various models, timescales, featurization techniques, and ML algorithms were compared. The best performing model used a time resolution of 2 ms, the longest time window investigated, and exhibited a F1-score of 0.95 with recall and accuracy of 1.0 and 0.94, respectively. Despite a decrease in accuracy at higher time resolutions, up to 93% of pores were still detected within 0.5 ms signal segments.

The two featurization strategies, PSD and HCTSA, yielded comparable performances. Both featurization approaches, to varying degrees, highlighted the superior effectiveness of the microphone over photodiode sensors and the off-axis photodiode over a coaxial geometry. PSD analysis illustrated that the acoustic and off-axis photodiode sensors both demonstrated a strong

correlation between oscillations around 30-35 kHz and keyhole pore creation events. The HCTSA-based models relied more heavily on the two photodiode sensors than the models using the PSD featurization. HCTSA analysis revealed that the degree of randomness in the acoustic, the stability metric of the off-axis photodiode, and the spectral content of the coaxial photodiode signal were the most salient properties to detect formation of the keyhole pores using the process monitoring signatures.

The developed workflows and models provide useful tools for pore identification and bring insight into keyhole pore formation signatures and mechanisms of various sensor signals. This paper reports results on single track scales, and therefore future work is required to deploy these methods during the production of full-scale L-PBF parts where the process complexity is significantly increased by the addition of powder and other defect formation types, such as lack of fusion pores.

CRediT authorship contribution statement

Sanam Gorgannejad: Conceptualization, Methodology, Formal Analysis, Investigation, Visualization, Writing – Original Draft, Writing – Review & Editing. **Aiden A. Martin:** Investigation, Writing – Review & Editing, Writing – Original Draft. **Jenny W. Nicolino:** Investigation, Writing – Review & Editing. **Maria Strantza:** Investigation, Writing – Review & Editing. **Gabriel M. Guss:** Investigation, Writing – Review & Editing. **Saad Khairallah:** Conceptualization, Writing – Review & Editing. **Jean-Baptiste Forien:** Investigation, Writing – Review & Editing. **Vivek Thampy:** Investigation, Writing – Review & Editing. **Sen Liu:** Investigation, Writing – Review & Editing. **Peiyu Quan:** Investigation, Writing – Review & Editing. **Christopher J. Tassone:** Investigation, Writing – Review & Editing. **Nicholas P. Calta:** Conceptualization, Investigation, Project Administration, Writing – Review & Editing.

Declaration of Competing Interest

The authors declare that they have no known competing financial interests or personal relationships that could have appeared to influence the work reported in this paper.

Acknowledgements

Use of the Stanford Synchrotron Radiation Lightsource, SLAC National Accelerator Laboratory, is supported by the U.S. Department of Energy, Office of Science, Office of Basic Energy Sciences under Contract No. DE-AC02-76SF00515. Lawrence Livermore National Laboratory is operated by Lawrence Livermore National Security, LLC, for the U.S. Department of Energy, National Nuclear Security Administration under Contract DE-AC52-07NA27344. Work at Lawrence Livermore was supported by the LLNL LDRD Program under project 21-ERD-008. The LLNL document release number is LLNL-JRNL-847264.

References

1. McCann, R., et al., In-situ sensing, process monitoring and machine control in Laser Powder Bed Fusion: A review. Additive Manufacturing, 2021. 45: p. 102058.
2. Grasso, M. and B.M. Colosimo, Process defects and in situ monitoring methods in metal powder bed fusion: a review. Measurement Science and Technology, 2017. 28(4): p. 044005.
3. Everton, S.K., et al., Review of in-situ process monitoring and in-situ metrology for metal additive manufacturing. Materials & Design, 2016. 95: p. 431-445.
4. Jensen, S.C., et al., Long-term process stability in additive manufacturing. Additive Manufacturing, 2023. 61: p. 103284.
5. Pokorný, P., et al., Porosity Analysis of Additive Manufactured Parts Using CAQ Technology. Materials (Basel), 2021. 14(5).
6. Ning, J., et al., Analytical modeling of part porosity in metal additive manufacturing. International Journal of Mechanical Sciences, 2020. 172: p. 105428.
7. Khairallah, S.A., T. Sun, and B.J. Simonds, Onset of periodic oscillations as a precursor of a transition to pore-generating turbulence in laser melting. Additive Manufacturing Letters, 2021. 1: p. 100002.
8. Bayat, M., et al., Keyhole-induced porosities in Laser-based Powder Bed Fusion (L-PBF) of Ti6Al4V: High-fidelity modelling and experimental validation. Additive Manufacturing, 2019. 30: p. 100835.
9. Kan, W.H., et al., A critical review on the effects of process-induced porosity on the mechanical properties of alloys fabricated by laser powder bed fusion. Journal of Materials Science, 2022. 57(21): p. 9818-9865.
10. Ye, D., et al., Defect detection in selective laser melting technology by acoustic signals with deep belief networks. The International Journal of Advanced Manufacturing Technology, 2018. 96(5): p. 2791-2801.
11. Shevchik, S.A., et al., Acoustic emission for in situ quality monitoring in additive manufacturing using spectral convolutional neural networks. Additive Manufacturing, 2018. 21: p. 598-604.
12. Imani, F., et al., Process Mapping and In-Process Monitoring of Porosity in Laser Powder Bed Fusion Using Layerwise Optical Imaging. Journal of Manufacturing Science and Engineering, 2018. 140(10).
13. Zhang, B., et al., In situ surface topography of laser powder bed fusion using fringe projection. Additive Manufacturing, 2016. 12: p. 100-107.
14. Gould, B., et al., In Situ Analysis of Laser Powder Bed Fusion Using Simultaneous High-Speed Infrared and X-ray Imaging. JOM, 2021. 73(1): p. 201-211.
15. Jason, C.F., M.L. Brandon, and Y. Ho. Measurement of process dynamics through coaxially aligned high speed near-infrared imaging in laser powder bed fusion additive manufacturing. in Proc.SPIE. 2017.
16. Cheng, B., et al., Melt pool sensing and size analysis in laser powder-bed metal additive manufacturing. Journal of Manufacturing Processes, 2018. 32: p. 744-753.
17. Martin, A.A., et al., Dynamics of pore formation during laser powder bed fusion additive manufacturing. Nature Communications, 2019. 10(1): p. 1987.
18. pandiyan, v., et al., Deep Learning-Based Monitoring of Laser Powder Bed Fusion Process on Variable Time-Scales Using Heterogeneous Sensing and Operando X-Ray Radiography Guidance. SSRN Electronic Journal, 2022.
19. Zhao, C., et al., Real-time monitoring of laser powder bed fusion process using high-speed X-ray imaging and diffraction. Scientific Reports, 2017. 7(1): p. 3602.
20. DePond, P.J., et al., Laser-metal interaction dynamics during additive manufacturing resolved by detection of thermally-induced electron emission. Communications Materials, 2020. 1(1): p. 92.
21. Chua, Z.Y., I.H. Ahn, and S.K. Moon, Process monitoring and inspection systems in metal additive manufacturing: Status and applications. International Journal of Precision Engineering and Manufacturing-Green Technology, 2017. 4(2): p. 235-245.
22. Spears, T.G. and S.A. Gold, In-process sensing in selective laser melting (SLM) additive manufacturing. Integrating Materials and Manufacturing Innovation, 2016. 5(1): p. 16-40.
23. Koester, L.W., et al., Acoustic monitoring of additive manufacturing for damage and process condition determination. AIP Conference Proceedings, 2019. 2102(1): p. 020005.
24. Taheri, H., et al., In Situ Additive Manufacturing Process Monitoring With an Acoustic Technique: Clustering Performance Evaluation Using K-Means Algorithm. Journal of Manufacturing Science and Engineering, 2019. 141(4).
25. Whiting, J., A. Springer, and F. Sciammarella, Real-time acoustic emission monitoring of powder mass flow rate for directed energy deposition. Additive Manufacturing, 2018. 23: p. 312-318.
26. Duley, W.W. and Y.L. Mao, The effect of surface condition on acoustic emission during welding of aluminium with CO2 laser radiation. Journal of Physics D: Applied Physics, 1994. 27(7): p. 1379.

27. Wasmer, K., et al., Laser processing quality monitoring by combining acoustic emission and machine learning: a high-speed X-ray imaging approach. Procedia CIRP, 2018. 74: p. 654-658.
28. Hossain, M.S. and H. Taheri, In Situ Process Monitoring for Additive Manufacturing Through Acoustic Techniques. Journal of Materials Engineering and Performance, 2020. 29(10): p. 6249-6262.
29. Wasmer, K., et al., In Situ Quality Monitoring in AM Using Acoustic Emission: A Reinforcement Learning Approach. Journal of Materials Engineering and Performance, 2019. 28(2): p. 666-672.
30. Liu, J. and P. Wen, Metal vaporization and its influence during laser powder bed fusion process. Materials & Design, 2022. 215: p. 110505.
31. Shevchik, S.A., et al., Deep Learning for In Situ and Real-Time Quality Monitoring in Additive Manufacturing Using Acoustic Emission. IEEE Transactions on Industrial Informatics, 2019. 15(9): p. 5194-5203.
32. Pandiyan, V., et al., Semi-supervised Monitoring of Laser powder bed fusion process based on acoustic emissions. Virtual and Physical Prototyping, 2021. 16: p. 481-497.
33. Tempelman, J.R., et al., Detection of keyhole pore formations in laser powder-bed fusion using acoustic process monitoring measurements. Additive Manufacturing, 2022. 55: p. 102735.
34. Forien, J.-B., et al., Detecting keyhole pore defects and monitoring process signatures during laser powder bed fusion: A correlation between in situ pyrometry and ex situ X-ray radiography. Additive Manufacturing, 2020. 35: p. 101336.
35. Mitchell, J.A., et al., Linking pyrometry to porosity in additively manufactured metals. Additive Manufacturing, 2020. 31: p. 100946.
36. Zouhri, W., et al., Optical process monitoring for Laser-Powder Bed Fusion (L-PBF). CIRP Journal of Manufacturing Science and Technology, 2020. 31: p. 607-617.
37. Jayasinghe, S., et al., Automatic quality assessments of laser powder bed fusion builds from photodiode sensor measurements. Progress in Additive Manufacturing, 2022. 7(2): p. 143-160.
38. Okaro, I.A., et al., Automatic fault detection for laser powder-bed fusion using semi-supervised machine learning. Additive Manufacturing, 2019. 27: p. 42-53.
39. Kong, L., et al., Multi-sensor measurement and data fusion technology for manufacturing process monitoring: a literature review. International Journal of Extreme Manufacturing, 2020. 2(2): p. 022001.
40. Tian, Q., et al., Deep Learning-Based Data Fusion Method for In Situ Porosity Detection in Laser-Based Additive Manufacturing. Journal of Manufacturing Science and Engineering, 2020. 143(4).
41. Gaikwad, A., et al., Multi phenomena melt pool sensor data fusion for enhanced process monitoring of laser powder bed fusion additive manufacturing. Materials & Design, 2022. 221: p. 110919.
42. Tempelman, J.R., et al., Sensor fusion of pyrometry and acoustic measurements for localized keyhole pore identification in laser powder bed fusion. Journal of Materials Processing Technology, 2022. 308: p. 117656.
43. Petrich, J., et al., Multi-modal sensor fusion with machine learning for data-driven process monitoring for additive manufacturing. Additive Manufacturing, 2021. 48: p. 102364.
44. Martin, A.A., et al., A laser powder bed fusion system for operando synchrotron x-ray imaging and correlative diagnostic experiments at the Stanford Synchrotron Radiation Lightsource. Review of Scientific Instruments, 2022. 93(4): p. 043702.
45. Ren, Z., et al., Machine learning-aided real-time detection of keyhole pore generation in laser powder bed fusion. Science, 2023. 379(6627): p. 89-94.
46. Sharma, G., K. Umapathy, and S. Krishnan, Trends in audio signal feature extraction methods. Applied Acoustics, 2020. 158: p. 107020.
47. Pandiyan, V., et al., Analysis of time, frequency and time-frequency domain features from acoustic emissions during Laser Powder-Bed fusion process. Procedia CIRP, 2020. 94: p. 392-397.
48. Mojahed Yazdi, R., F. Imani, and H. Yang, A hybrid deep learning model of process-build interactions in additive manufacturing. Journal of Manufacturing Systems, 2020. 57: p. 460-468.
49. Ghayoomi Mohammadi, M., D. Mahmoud, and M. Elbestawi, On the application of machine learning for defect detection in L-PBF additive manufacturing. Optics & Laser Technology, 2021. 143: p. 107338.
50. Zhao, C., et al., Critical instability at moving keyhole tip generates porosity in laser melting. Science, 2020. 370(6520): p. 1080-1086.
51. Calta, N.P., et al., An instrument for in situ time-resolved X-ray imaging and diffraction of laser powder bed fusion additive manufacturing processes. Review of Scientific Instruments, 2018. 89(5).
52. Solomon, J.O.M., PSD computations using Welch's method. [Power Spectral Density (PSD)]. 1991: United States.

53. Caprio, L., A.G. Demir, and B. Previtali, Observing molten pool surface oscillations during keyhole processing in laser powder bed fusion as a novel method to estimate the penetration depth. Additive Manufacturing, 2020. 36: p. 101470.
54. Parhi, K.K. and M. Ayinala, Low-Complexity Welch Power Spectral Density Computation. IEEE Transactions on Circuits and Systems I: Regular Papers, 2014. 61(1): p. 172-182.
55. Welch, P., The use of fast Fourier transform for the estimation of power spectra: A method based on time averaging over short, modified periodograms. IEEE Transactions on Audio and Electroacoustics, 1967. 15(2): p. 70-73.
56. Fulcher, B.D. and N.S. Jones, hctsa: A Computational Framework for Automated Time-Series Phenotyping Using Massive Feature Extraction. Cell Systems, 2017. 5(5): p. 527-531.e3.
57. Li, J., et al., Data-Driven Fault Detection and Classification for MTDC Systems by Integrating HCTSA and Softmax Regression. IEEE Transactions on Power Delivery, 2022. 37(2): p. 893-904.
58. O'Connor, T., S. Santaniello, and B. Javidi, COVID-19 detection from red blood cells using highly comparative time-series analysis (HCTSA) in digital holographic microscopy. Optics Express, 2022. 30(2): p. 1723-1736.
59. Yang, X., et al., pH-Responsive Biomimetic Polymeric Micelles as Lymph Node-Targeting Vaccines for Enhanced Antitumor Immune Responses. Biomacromolecules, 2020. 21(7): p. 2818-2828.
60. Struchtrup, A.S., D. Kvaktun, and R. Schiffers, Comparison of feature selection methods for machine learning based injection molding quality prediction. AIP Conference Proceedings, 2020. 2289(1): p. 020052.
61. Gletsos, M., et al., A computer-aided diagnostic system to characterize CT focal liver lesions: design and optimization of a neural network classifier. IEEE Transactions on Information Technology in Biomedicine, 2003. 7(3): p. 153-162.
62. Jain, A.K., R.P.W. Duin, and M. Jianchang, Statistical pattern recognition: a review. IEEE Transactions on Pattern Analysis and Machine Intelligence, 2000. 22(1): p. 4-37.
63. Zio, E., P. Baraldi, and N. Pedroni, Selecting features for nuclear transients classification by means of genetic algorithms. IEEE Transactions on Nuclear Science, 2006. 53(3): p. 1479-1493.
64. Castanedo, F., A Review of Data Fusion Techniques. The Scientific World Journal, 2013. 2013: p. 704504.
65. Meng, T., et al., A survey on machine learning for data fusion. Information Fusion, 2020. 57: p. 115-129.
66. Luts, J., et al., A tutorial on support vector machine-based methods for classification problems in chemometrics. Analytica Chimica Acta, 2010. 665(2): p. 129-145.
67. MurtiRawat, R., et al. Breast Cancer Detection Using K-Nearest Neighbors, Logistic Regression and Ensemble Learning. in 2020 International Conference on Electronics and Sustainable Communication Systems (ICESC). 2020.
68. Tohka, J. and M. van Gils, Evaluation of machine learning algorithms for health and wellness applications: A tutorial. Computers in Biology and Medicine, 2021. 132: p. 104324.
69. Luko, S., A Review of the Weibull Distribution and Selected Engineering Applications. 1999.
70. Azodi, C.B., J. Tang, and S.-H. Shiu, Opening the Black Box: Interpretable Machine Learning for Geneticists. Trends in Genetics, 2020. 36(6): p. 442-455.

Appendix A. Hyperparameter Optimization and SFFS Results

The results of the hyperparameter optimization for the KNN and GNB models are presented in this section. The naïve grid search was performed over a range of hyperparameters, and the best combination was selected based on the highest 5-fold cross-validation score. The tuned hyperparameter for the KNN models was the number of neighbors (*K*). The GNB algorithm uses a smoothing hyperparameter (*var_smoothing*) to improve the stability of the calculations in situations where one or more of the feature variances is minimal. It can be tuned to optimize the performance of the model on a particular dataset. Table A.1. presents the tuned hyperparameters for the PSD and HCTSA models used to carrying out the SFFS algorithm. The resulting optimized feature sets obtained through the SFFS procedure are detailed in Table A.2.

Table A.1. Tuned hyperparameters of the PSD and HCTSA models.

	PSD			HCTSA		
	2 ms	1 ms	0.5 ms	2 ms	1 ms	0.5 ms
KNN (*K*)	20	5	11	10	11	4
GNB (*var_smoothing*)	0.01	1	1e-3	1e-10	1e-4	1e-3

Table A.2. Size of the optimal fused feature banks identified by the SFFS algorithm.

	PSD			HCTSA		
	2 ms	1 ms	0.5 ms	2 ms	1 ms	0.5 ms
SVM	27	28	32	14	30	30
KNN	16	21	30	15	18	25
GNB	13	14	16	20	25	26

Appendix B. Top 20 Sensor Features used to Develop the Machine Learning Models

The TS_TopFeatures()function identifies the top features that accurately distinguish classes of time series. The top 20 HCTSA acoustic, off-axis, and coaxial photodiode features can be found in Table B.1. through Table B.3. The full definition of the abbreviated feature descriptions is provided elsewhere[1].

The uncertainty and randomness of the acoustic signals are quantified by computing the statistics of the estimated probability density function (PDF) of the signals obtained through kernel smoothing method (DN features), the distributional signal entropy (EN features), and the auto-mutual information of signal distribution (CO features).

[1]https://hctsa-users.gitbook.io/hctsa-manual/list-of-included-code-files

Table B.1. Top 20 HCTSA acoustic features

	Acoustic		
	2 ms	1 ms	0.5 ms
1	MD_rawHRVmeas_SD2	mean_absolute_deviation	standard_deviation
2	DN_FitKernelSmoothraw_entropy	standard_deviation	mean_absolute_deviation
3	standard_deviation	MD_rawHRVmeas_SD2	MD_rawHRVmeas_SD2
4	interquartile_range	interquartile_range	interquartile_range
5	mean_absolute_deviation	DN_FitKernelSmooth_ncross_03	DN_FitKernelSmooth_ncross_03
6	median_absolute_deviation	median_absolute_deviation	DN_FitKernelSmoothraw_entropy
7	EN_DistributionEntropy_raw_ks__001	DN_FitKernelSmooth_area_02	median_absolute_deviation
8	NL_nsamdf_1_14_05_1_7_L	DN_FitKernelSmooth_area_03	DN_FitKernelSmooth_area_02
9	DN_FitKernelSmooth_area_03	DN_FitKernelSmooth_area_01	DN_FitKernelSmooth_area_03
10	CO_HistogramAMI_even_5bin_ami1	MD_rawHRVmeas_SD1	MD_rawHRVmeas_SD1
11	EN_DistributionEntropy_raw_ks__002	DN_FitKernelSmoothraw_entropy	DN_FitKernelSmooth_area_01
12	FC_LocalSimple_1fit2_meanabserr	CO_AddNoise_1_even_10_meanch	NL_nsamdf_1_14_05_1_7_L
13	EN_DistributionEntropy_raw_ks__005	CO_AddNoise_1_even_10_fitlinb	DN_FitKernelSmoothraw_max
14	CO_glscf_2_2_1	SB_MotifThree_diffquant_aaa	EN_DistributionEntropy_raw_ks__01
15	MD_rawHRVmeas_SD1	CO_HistogramAMI_even_10bin_ami1	EN_DistributionEntropy_raw_ks__005
16	CO_StickAngles_y_ac1_n	SB_MotifThree_quantile_hh	EN_DistributionEntropy_raw_ks__03
17	DN_FitKernelSmooth_ncross_03	CO_AddNoise_1_std1_10_fitlinb	EN_DistributionEntropy_raw_ks__02
18	CO_StickAngles_y_tau_all	SB_MotifTwo_diff_uuuu	DN_FitKernelSmooth_area_005
19	CO_StickAngles_y_ac1_all	CO_AddNoise_1_quantiles_10_fitlinb	DN_FitKernelSmooth_arcl_2
20	CO_glscf_1_2_1	CO_AddNoise_1_even_10_fitexpa	DN_CompareKSFit_uni_psy

To assess the stability of the off-axis photodiode signals, HCTSA computes the decay rate of the sum, mean, and maximum of diagonal elements of the transition matrices, changes in symmetry, and the eigenvalues of the transition matrix (SB features).

Table B.2. Top 20 HCTSA off-axis photodiode features

	Off-axis Photodiode		
	2 ms	1 ms	0.5 ms
1	EN_DistributionEntropy_raw_ks__005	FC_Surprise_dist_5_2_udq_500_std	FC_LocalSimple_1fit5_taures
2	DN_CompareKSFit_uni_psy	DN_FitKernelSmoothraw_max	SB_TransitionpAlphabet_40_1_maxeig_fexpb
3	MD_pNN_raw_pnn5	SB_TransitionpAlphabet_40_1_maxeig_fexpa	SB_TransitionpAlphabet_40_1_maxeig_fexpa
4	SB_MotifTwo_diff_duud	SB_TransitionpAlphabet_40_1_maxeig_fexpr2	SB_MotifTwo_diff_duud
5	SB_MotifTwo_diff_udd	EN_DistributionEntropy_raw_ks__02	DN_FitKernelSmoothraw_max
6	EN_DistributionEntropy_raw_ks__02	SB_MotifTwo_diff_duud	FC_LocalSimple_mean2_ac2
7	SB_TransitionpAlphabet_40_1_maxeig_fexpa	SB_TransitionpAlphabet_40_1_maxeig_fexpb	SB_TransitionpAlphabet_40_1_maxeig_fexpr2
8	EN_DistributionEntropy_raw_ks__01	propUnique	SB_TransitionpAlphabet_40_1_maxeig_fexprmse
9	DN_FitKernelSmoothraw_max	EN_DistributionEntropy_raw_ks__03	EN_DistributionEntropy_raw_ks__01
10	SB_TransitionpAlphabet_40_1_maxeig_fexpr2	DN_CompareKSFit_uni_psy	propUnique
11	SB_MotifTwo_diff_ddu	PH_Walker_momentum_5_sw_propcross	EN_DistributionEntropy_raw_ks__02
12	SB_MotifThree_diffquant_aac	SB_MotifThree_diffquant_bbcc	DN_FitKernelSmoothraw_entropy
13	EN_DistributionEntropy_raw_ks__03	SB_TransitionpAlphabet_40_1_maxeig_fexprmse	EN_DistributionEntropy_raw_ks__03
14	SB_TransitionpAlphabet_40_1_maxeig_fexpb	EN_DistributionEntropy_raw_ks__01	PH_Walker_momentum_2_w_std
15	SB_TransitionpAlphabet_40_1_maxeig_fexprmse	SB_MotifThree_diffquant_aac	EN_DistributionEntropy_raw_ks__005
16	PH_Walker_momentum_5_sw_propcross	DN_FitKernelSmoothraw_entropy	EN_DistributionEntropy_raw_ks__03
17	DN_FitKernelSmoothraw_entropy	FC_LocalSimple_1fit5_taures	EN_DistributionEntropy_raw_ks__02
18	NW_VisibilityGraph_norm_modek	SB_MotifTwo_diff_uddu	DN_FitKernelSmooth_area_005
19	median_absolute_deviation	PH_Walker_momentum_2_sw_propcross	DN_FitKernelSmooth_arcl_2
20	propUnique	EN_PermEn_4_2_normPermEn	DN_CompareKSFit_uni_psy

The top coaxial photodiode features recover several spectral measures (SC features). The frequency content is determined through the use of periodograms, fast Fourier based transformations (SP features), and continuous wavelet transform (WL features) to obtain the signal spectrum.

Table B.3. Top 20 HCTSA coaxial photodiode features

	Coaxial Photodiode		
	2 ms	1 ms	0.5 ms
1	SP_Summaries_welch_rect_fpoly2_sse	PP_Compare_rav10_swss10_2	PP_Compare_rav2_swss10_2
2	SP_Summaries_fft_fpoly2_sse	WL_cwt_db3_32_gam2	PP_Compare_rav3_swss10_2
3	SC_FluctAnal_2_dfa_50_1_3_logi_ssr	WL_cwt_db3_32_dd_SC_h	PP_Compare_medianf10_swss10_2
4	SC_FluctAnal_mag_2_dfa_50_2_logi_se1	SC_FluctAnal_sign_2_dfa_50_2_logi_alpha	PP_Compare_medianf4_swss10_2
5	SC_FluctAnal_mag_2_dfa_50_2_logi_se2	WL_cwt_db3_32_stat_5_m_s	WL_cwt_db3_32_gam2
6	SC_FluctAnal_2_dfa_50_1_logi_se1	PP_Compare_rav10_swss10_1	PP_Compare_medianf4_swss10_1
7	SC_FluctAnal_2_dfa_50_1_logi_se2	WL_cwt_db3_32_gam1	WL_cwt_sym2_32_min_ssc
8	SC_FluctAnal_2_dfa_50_1_2_logi_se1	NW_VisibilityGraph_norm_kac3	NW_VisibilityGraph_norm_iqrk
9	SC_FluctAnal_2_dfa_50_1_2_logi_se2	WL_cwt_db3_32_SC_h	SB_TransitionpAlphabet_40_1_maxdiagfexp
10	SP_Summaries_welch_rect_fpoly2_rmse	MF_GP_LocalPrediction_covSEiso_covNoise_5_3_10_beforeafter_stdmlik	AC_nl_44
11	SP_Summaries_fft_fpoly2_rmse	WL_cwt_sym2_32_min_ssc	PP_Compare_rav4_swss10_2
12	SC_FluctAnal_2_dfa_50_1_logi_ratsplitminerr	WL_cwt_sym2_32_gam1	PP_Compare_medianf10_swss5_1
13	CO_CompareMinAMI_even_2_80_median	PP_Compare_rav4_swss10_1	NL_crptool_fnn_10_2_mi_firstunder005
14	NW_VisibilityGraph_norm_iqrk	MF_GP_LocalPrediction_covSEiso_covNoise_5_3_10_beforeafter_maxmlik	SC_FluctAnal_sign_2_dfa_50_2_logi_alpha
15	SB_BinaryStats_mean_stdstretchdiff	WL_cwt_sym2_32_gam2	PP_Compare_rav10_kscn_olapint
16	SC_FluctAnal_2_rsrangefit_50_1_logi_stdssr	WL_cwt_sym2_32_stat_5_m_s	PP_Compare_rav3_swss10_1
17	CO_CompareMinAMI_even_2_80_mean	WL_cwt_db3_32_min_ssc	NW_VisibilityGraph_norm_kac3
18	SC_FluctAnal_2_rsrange_50_logi_se1	SC_FluctAnal_2_dfa_50_2_logi_meanssr	MD_rawHRVmeas_SD2
19	SC_FluctAnal_2_rsrange_50_logi_se2	SC_FluctAnal_2_dfa_50_3_logi_se1	EN_PermEn_4_2_normPermEn
20	coeff_var_2	SC_FluctAnal_2_dfa_50_3_logi_se2	MF_GP_LocalPrediction_covSEiso_covNoise